Applied Physics Letters

RESEARCH ARTICLE | DECEMBER 18 2023

High-resolution spectroscopic imaging of atoms and nanoparticles in thin film vaporization

Special Collection: Plasma Sources for Advanced Semiconductor Applications

D. J. Engels ; R. A. Meijer ; H. K. Schubert ; W. J. van der Zande ; W. Ubachs ; O. O. Versolato

Check for updates

Appl. Phys. Lett. 123, 254102 (2023)
https://doi.org/10.1063/5.0173871

View Online
Export Citation
CrossMark

04 January 2024 12:56:13

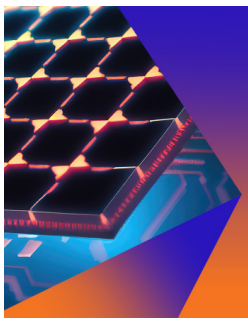

Applied Physics Letters
Special Topic:
Hybrid and Heterogeneous Integration in Photonics: From Physics to Device Applications
Submit Today
AIP Publishing

AIP Publishing

High-resolution spectroscopic imaging of atoms and nanoparticles in thin film vaporization

Cite as: Appl. Phys. Lett. **123**, 254102 (2023); doi: 10.1063/5.0173871
Submitted: 25 August 2023 · Accepted: 24 November 2023 ·
Published Online: 18 December 2023

View Online Export Citation CrossMark

D. J. Engels,[1,2,3,a)] R. A. Meijer,[1,2] H. K. Schubert,[1,2] W. J. van der Zande,[1] W. Ubachs,[1,2] and O. O. Versolato[1,2]

AFFILIATIONS

[1]Advanced Research Center for Nanolithography, Science Park 106, 1098 XG Amsterdam, The Netherlands
[2]Department of Physics and Astronomy and LaserLab, Vrije Universiteit Amsterdam, De Boelelaan 1081, 1081 HV Amsterdam, The Netherlands
[3]Department of Applied Physics, Eindhoven University of Technology, Den Dolech 2, 5600 MB Eindhoven, The Netherlands

Note: This paper is part of the Special Topic: Plasma Sources for Advanced Semiconductor Applications.
[a)]**Author to whom correspondence should be addressed:** d.engels@arcnl.nl

ABSTRACT

We introduce a spectroscopic absorption imaging method in the UV regime (225–400 nm) to study tin vapor created by irradiating a thin film with a low intensity 10^8 W cm^{-2} nanosecond laser pulse, a case inspired by current developments around "advanced target shaping" in industrial laser-produced plasma sources for extreme ultraviolet light. The 4-ns-time-resolved, 10-μm-spatial-resolution images contain a 10-cm^{-1}-resolution spectrum of the vapor in each pixel 100 ns after the vaporization. The images allow us to reveal a homogeneous temperature profile throughout the vapor of around 3000 K. We obtain a density map of the atoms (with a peak density of 5×10^{18} cm^{-3}) and nanoparticles (10^{12} cm^{-3} for the best fitting 20 nm radius case), which both are shown to be present in the vapor. For each free atom, approximately three appear to be clustered in nanoparticles, and this composition is invariant over space and density. The density and temperature maps of the free atoms are combined to estimate the electron density (peaking at 10^{13} cm^{-3}) in the vapor.

© 2023 Author(s). All article content, except where otherwise noted, is licensed under a Creative Commons Attribution (CC BY) license (http://creativecommons.org/licenses/by/4.0/). https://doi.org/10.1063/5.0173871

Optical diagnostics of plasma and vapor play a key role in the development of modern technologies. Notable examples include recent breakthroughs in tokamak fusion plasma, where multiplexed imaging provides necessary detail, e.g., of the scrape-off layer,[1–4] and EUV lithography, where active and passive spectroscopy methods led to key new insights.[5–7] The diagnostics employed so far have focused either on spectroscopic resolution, to identify contributing electronic states in atoms and ions, or on imaging resolution, to, e.g., pinpoint the precise location of high-temperature plasma areas.[8,9] This focus typically comes with tradeoffs between imaging and spectroscopic resolution or with the necessity to employ tedious spatial raster scans to combine sufficient resolution on both fronts.[10–13] The use of liquid tin as laser-plasma targets in EUV lithography[14,15] and plasma divertor shielding in fusion[16–18] motivates the development of direct optical diagnostics that combine high spatial and temporal resolution with high-resolution spectroscopy of tin vapor that may comprise atoms as well as nanoparticles.

In this work, we introduce a method of UV spectroscopic absorption imaging that combines ∼10 μm spatial, 4 ns temporal, and a 10 cm^{-1} spectroscopic resolution that enables identifying the composition of tin vapor. We develop and apply the method to the field of tin target shaping, relevant to the production of EUV light using laser-produced plasma (LPP).[15] Specifically, we use a 10^8 W/cm^2 nanosecond-duration laser pulse to experimentally create a vapor from a thin film, which is imaged using the method, and to determine the vapor's state of matter. Target shaping, i.e., creating thin tin sheets from droplets, is used for the LPPs to increase EUV generation efficiency.[19] Even larger efficiency gains, in converting more laser light into useful EUV photons, could be obtained with improved, advanced target shaping.[20] Inspired by this concept, we here investigate targets pre-shaped by a further laser pulse to create a tin vapor[21] that may improve the interaction with the main pulse and increase the conversion efficiency (analogous to the pre-plasma suggested in Refs. 22 and 23).

In the experiment (see Fig. 1), a train of tin microdroplets ($T = 270$ °C in the current experiments) is generated using a droplet generator mounted on top of a vacuum chamber (10^{-7} mbar). The droplet stream passes through a sheet of light a few millimeters above the vacuum chamber center. Scattered light at a kilohertz rate is picked up by a photo-multiplier tube and downsampled to 5 Hz to trigger the

04 January 2024 12:56:13

© Author(s) 2023

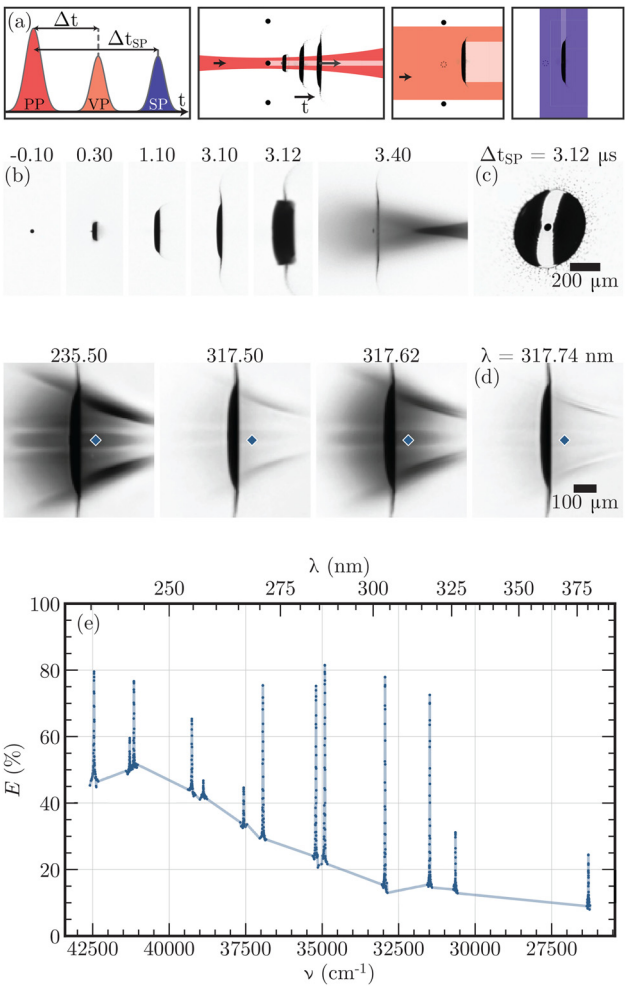

FIG. 1. (a) Time-ordering of the three laser pulses used in the experiment. First, the tin microdroplet is hit by a pre-pulse (PP), propelling the droplet, and expanding it into a thin film. At a set time (Δt), this thin film is irradiated with the vaporization pulse (VP), creating the tin vapor. The tin vapor is imaged using the shadowgraphy pulse (SP). (b) Processed side-view shadowgrams created with 284.08 nm-backlighting at different times after the PP. The VP hits 3.1 μs after the PP. (c) Front view of the thin film (at 30°, showing the line focus of the VP, to control absorption path length). (d) Side-view shadowgrams at various SP wavelengths, 100 ns after the VP. (e) Extinction (E) spectrum for the location indicated by the blue dot in panel (d).

experiment. For more details of the experimental setup, see previous works.[21,24]

A microdroplet (diameter set to ∼30 μm) is first hit by the pre-pulse [PP, 10 ns, $\lambda = 1064$ nm, cf. Ref. 25, and see Fig. 1(a)]. Spatially, the PP is focused to a Gaussian spot size of approximately 100 × 100 μm (FWHM, full-width at half-maximum). The droplet is propelled by the PP and expands into a thin sheet.[24,26]

At a set time after the PP, here, 3.1 μs, the sheet is irradiated with a 0.5 mJ ns-length vaporization pulse (VP, $\lambda = 1064$ nm). At this time, the sheet has a thickness of 50–20 nm (decreasing radially outward).[21] The VP is focused to a *line* focus using a cylindrical lens and has an FWHM of 1100 × 70 μm, to define a common interaction length of the side-view shadowgraphy. The energy of the VP is carefully tuned to ensure vaporization occurs without significant ionization of the tin as evidenced by the absence of any signal on Faraday cup ion detectors.

Finally, the vapor is imaged using two synchronous shadowgraphy pulses (SPs). A front-view image (at 30°) is taken using 560 nm light to check proper droplet-to-laser alignment.[21] The light for the side-view image at 90° comes from a Continuum Horizon OPO laser here generating wavelengths between 225 and 400 nm, with a pulse length of 4 ns, a spectral bandwidth of 5–10 cm^{-1}, and a spatial resolution of between 5 and 10 μm depending on the wavelength, respectively. Figure 1(b) shows the evolution of the tin target from microdroplet to vapor using side-view UV shadowgraphy, while Fig. 1(c) shows the front view from the green shadowgraphy after the VP has hit.

For each UV shadowgraphy wavelength, we average over 50 frames (in our stroboscopic method, each frame corresponds to a different droplet), after correcting for minor tilt and alignment changes. This reduces the visibility of coherence "speckle" and increases the signal-to-noise ratio. The images obtained at different wavelengths are scaled to a global magnification value (magnification changes with wavelength due to the chromatic, single-lens-imaging setup). All CCD pixels are binned into 4 × 4 bins (in the following referred to as a pixel) to reduce the impact of any remaining misalignment, resulting in an effective spatial resolution of 10 μm. Figure 1(d) highlights the range of wavelengths allowed by the OPO laser and the changing contrast of the vapor. These and all subsequent images are taken with 100 ns between the VP and the shadowgraphy.

Figure 1(e) shows the extinction spectrum for the location indicated by the blue marker in panel (d). A broadband contribution is present, decreasing toward longer wavelengths. This we attribute to the presence of nanoparticles as we will describe below.[27–29]

Furthermore, strong Sn-I atomic resonances are visible, proving the presence of free atoms in the vapor (see the supplementary material Note 1 for an overview of resonances).[30–32] The electronic levels probed can be seen in the Grotrian diagram in Fig. 2(a). These atomic resonances enable the extraction of the temperature of the vapor using a Boltzmann plot.[6,33] To do so, the broadband contribution is removed to obtain the atomic contribution to the extinction spectrum, E_{atom} [see Fig. 2(b)]. Next, we calculate the area under the logarithm of E_{atom} for each atomic resonance and use this as the metric for the line strength S. This line strength can be related to the Boltzmann population fraction $b(T)$,

$$S \equiv \int -\ln(1 - E(\nu))d\nu = n_0 L \chi(\nu) b(T) \sigma_0. \quad (1)$$

Here, σ_0 is the base resonance cross section (see supplementary material Table S1), n_0 is the total atom density, L is the common path length through the vapor [∼100 μm, obtained from images like Fig. 1(c)], and taking $\chi(\nu)$ as a common broadening factor. Plotting S vs σ_0 gives a straight line, of which the slope is set by the Boltzmann population fraction [see Fig. 2(c)].

We assume that no other higher-lying levels than those shown in the Grotrian diagram are occupied (the next level lies at 17 162 cm^{-1}). This allows us to calculate the occupation of the levels based on the fit slopes, with the common factors n_0, L, and $\chi(\nu)$ dividing out and, thus, our treatment is independent of their specific numerical values.

04 January 2024 12:56:13

© Author(s) 2023

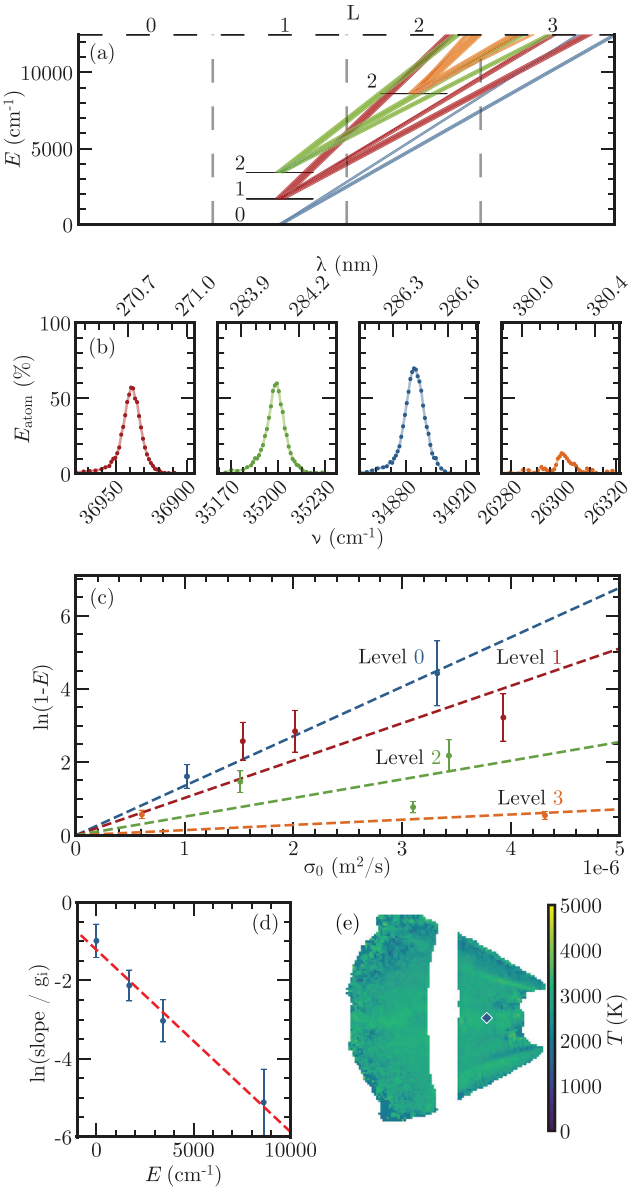

FIG. 2. (a) Grotrian diagram. Only the ground level of neutral tin $5s^25p^2$ is shown for clarity. The four energy levels probed in the experiment are also shown. The different colored lines are resonances from these levels to higher levels (not shown). The numbers next to the levels indicate the total angular momentum quantum number *J*. (b) Extinction around several atomic resonances when the broadband term is subtracted (E_{atom}). The plot colors relate to the ground levels of the resonances in panel (a). (c) σ_0 vs $\ln(1-E)$ integrated over the resonance. See the main text for information. (d) Boltzmann plot with fit of the four levels based on the slopes in panel (c) for the pixel indicated in panel (e). (e) Resulting temperature map for the entire vapor.

These occupations are then fit with a Boltzmann distribution, resulting in a temperature [see Fig. 2(d)].

Having demonstrated the process above for a single pixel, we next apply it to the full image to create a temperature map. The result, presented in Fig. 2(e), reveals a relatively uniform temperature around 3000 K. Small deviations from a homogeneous temperature can be seen in high-extinction areas [cf. Fig. 1(d)]. These deviations may point to temperature increases in colliding vapor flows or potentially to differences in $\chi(\nu)$ between resonances becoming more apparent at high densities. In general, both (i) the non-trivial spectral shape of the OPO laser and (ii) the uncertainty in the assumption of constant density broadening contribute to a conservative overall systematic uncertainty of approximately 20% on the data points in Fig. 2(c). This uncertainty propagates through the fit [cf. Fig. 2(d)] to result in an uncertainty in the order of 100 K in temperature *T* [Fig. 2(e)]. With this in mind, we note that the temperature can be considered to be relatively uniform and close to the boiling temperature of tin of 2875 K.

Having obtained the overall temperature map, we next extract the local density, which together with the temperature and the composition defines the state of matter of the target material. Figure 3 shows extinction spectra for selected locations, indicated by the dots in Figs. 3(a)–3(c). As shown in Fig. 3(d), the individual spectra are very similar, with the only clear difference being the total extinction. This similarity can be further investigated by introducing the relative density (*a*) and relative cross section (σ_{rel}). To do so, Beer–Lambert's law[34,35] is inverted to an equation for the cross section: $\sigma(\nu) = -\ln(1-E(\nu))/nL$. Again, *n* is the density of the material and σ its extinction (absorption + scattering) cross section, and *L* is the (common) path length through the material.

A relative density *a* can be defined for any two pixels in an image by comparing the $\ln(1-E(\nu))$ between the two locations, following Schupp *et al.*[36] The advantage of relative densities is that we do not require any underlying model for the cross section. Figure 3(e) shows $\ln(1-E(\nu))$ to highlight the non-linearity of Beer–Lambert; the atomic resonances become more pronounced when taking the logarithm since these have very high extinction values.

We fit the broadband extinction spectrum of each pixel to the spectrum of a single reference pixel (defined as $a=1$), obtaining a single (wavelength independent, unitless) value *a*: an overall multiplicative factor that minimizes the difference between the individual spectra of panel (e) and the reference spectrum. Figure 3(f) shows the result of the fit procedure for the selected positions expressed as a relative cross section, σ_{rel}, defined as $\sigma_{rel}(\nu) = -\ln(1-E(\nu))/a$. We set $\sigma_{rel}(\nu) = 1$ for the reference pixel at the longest wavelength (381 nm).

Figure 3(g) shows the same results with the atomic resonances filtered out for improved visibility. In addition to the selected locations, the mean σ_{rel} with uncertainty bounds are also plotted to highlight the collapse of *every pixel* in the vapor to the same curve. With this, we reveal the striking fact that the spectra are spatially invariant and, thus, the underlying nanoparticle size distribution that causes the broadband extinction curve is the same everywhere in the vapor.

We next plot the values obtained for *a* in Fig. 3(b), showing a strong correlation with the original shadowgraph in panel (a). An atomic equivalent to the method above can be defined by comparing the area under the logarithm of E_{atom} [following Fig. 2(c)] between different pixels to again obtain a single *a* as an overall multiplicative factor. The results are presented in Fig. 3(c). Remarkably, the two means for obtaining the relative densities *a* produce extremely similar spatial profiles, comparing panels (b) and (c). This indicates that the nanoparticles and free atoms move together and that the densities, ranging over an order of magnitude, have no influence on the composition of the vapor itself—the composition appears to be frozen in.

04 January 2024 12:56:13

© Author(s) 2023

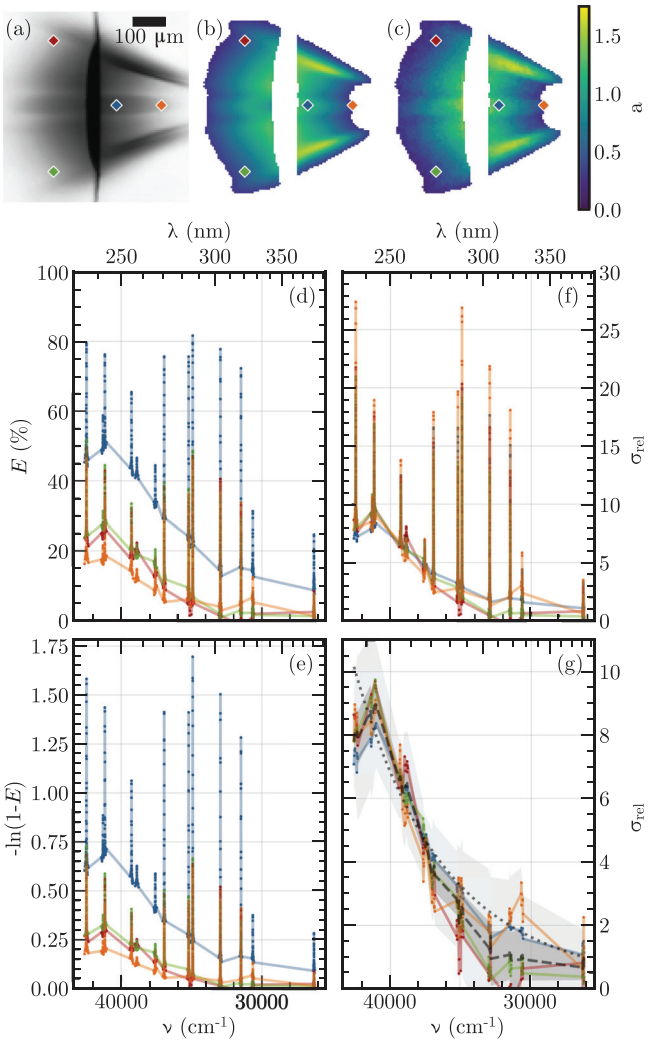

FIG. 3. (a) Image of the vapor at 284.08 nm (on an atomic resonance). Four different locations for which the curves are shown in (d)–(g) are indicated. (b) and (c) Relative, unitless, densities *a* determined using the broadband extinction curve (b) or the atomic resonances (c). (d) Extinction for the four locations. (e) $-\ln(1-E)$ for the four locations. (f) Relative cross section (σ_{rel}) for the four locations. (g) Relative cross section (atomic resonances filtered out). Mean (gray, dashed) for all pixels and uncertainty bounds (at 1 and 3 standard deviations, gray shading) are also indicated. The dotted gray line indicates the best-fitting nanoparticle radius of 20 nm.

The total number of atoms in the vapor can be estimated, taking as input the known cross section of the resonances and the constant path length (100 μm). Furthermore, we take a linear scaling of the broadening $\chi(\nu)$ with density.[37] Using this, an absolute density map can be obtained [which is indistinguishable from Fig. 3(c) and, therefore, not shown] and peaks at $5 \times 10^{18}\,\mathrm{cm}^{-3}$. Summing over the full map (i.e., integrating over the entire measured volume) results in a total number of 1×10^{13} atoms in the vapor. This number represents approximately 40% of the total number of vaporized atoms when compared to the prediction from the sheet thickness model of Liu *et al.*[21]

A similar estimate can be made for the broadband component of the spectrum caused by nanoparticles. We use a numerical code[38] (cross-checked with an alternative code[39]) for Mie theory[27,28] to obtain extinction cross sections, which includes both absorption and scattering, for nanoparticles (typically valid for sizes above 40–100 atoms, a radius of 1–3 nm).[29,40,41] Refractive index data are taken from Cisneros *et al.*[42] and extrapolated to wavelengths below 310 nm (4 eV) using a Drude-model fit.[43] The dotted gray line in Fig. 3(g) indicates the best-fitting nanoparticle radius of approximately 20 nm, obtained from a least squares fit of the cross section predicted by Mie theory to the collapsed relative cross section, with the particle radius being the single free fit parameter. We note that Mie extinction has near-equal contributions from absorption and scattering in this size regime. A nanoparticle density of approximately $10^{12}\,\mathrm{cm}^{-3}$ is obtained when taking the σ of a 20 nm radius nanoparticle. This means that a total number of $3(1) \times 10^{13}$ atoms are clustered in nanoparticles to create the broadband spectrum, which is close to the total number of atoms in the vaporized thin film (3×10^{13}).

The dominant uncertainties pertain to (i) the extrapolated refractive index and (ii) the estimated number of vaporized atoms. More atoms may be vaporized from parts of the thin film that did not become transparent after the laser pulse. Additionally, the atomic broadening, hidden by the complex spectral shape of the UV laser, adds uncertainty to the atomic density calculation.

Critically, we learn from this that for every free atom, several others (approximately three) are clustered in nanoparticles. We note that this estimate is relatively independent of the precise radius of the nanoparticles, with the cross section per atom being relatively constant in this range. This independence extends to below the strict validity range of Mie theory as well, providing strong support for the statement that only one out of three atoms are "free" with the remainder bound in nanoparticles.[29]

The obtained densities and temperatures of the atoms can be combined to obtain a local electron density (which is an important quantity for laser absorption in media, and thus, for the industrial application of EUV generation) within the vapor using the Saha–Boltzmann equation.[44] Given the rather uniform temperature profile [cf. Fig. 2(e)], this local electron density closely follows Fig. 3(c) and yields a maximum electron density of approximately $10^{13}\,\mathrm{cm}^{-3}$, six orders of magnitude below the critical electron density for a 10 μm-wavelength CO_2 main pulse. Only under EUV-generating conditions, when high tin charge states (Sn^{10+}–Sn^{14+}) are generated, the atomic vapor reach the critical density—enabling sustaining the plasma, with laser light absorbed via the inverse Bremsstrahlung mechanism,[45] but not explaining its "ignition." The current vapor could still offer an effective advanced target in EUV sources given that nanoparticles may instead ignite the plasma, leading to rapid ionization and the formation of a critical surface. Additionally, the increased laser-material interaction length scale may promote laser absorption.

In addition to the value of our method to diagnose tin vapor targets, the observed broadband extinction spectrum with its spatial invariance and density independence may provide insight into the vapor production mechanism. Two well-known mechanisms are (i) Hertz–Knudsen evaporation and (ii) homogeneous nucleation (also known as phase explosion or explosive boiling).[46–51] Our detailed calculations (see the supplementary material Note 2) indicate that vaporization following the Hertz–Knudsen equation can explain the

04 January 2024 12:56:13

© Author(s) 2023

observed rate of double-sided vaporization (dividing the typical thickness ~25 nm by the 6 ns VP pulse length[21]) when taking as input the tin vapor pressure in vacuum[52,53] and assuming a surface temperature of approximately 4000 K. We note that this temperature, while sufficient to explain the observed vaporization rate, lies well below the thermodynamic critical temperature (which is between 7073 and 8800 K for tin[54,55]) and is very close to the observed late-time temperature obtained from Fig. 2. Since vaporization following the Hertz–Knudsen model only describes the formation of free atoms,[49,51] any nanoparticles must have been formed through coalescence processes which we may hypothesize to lead to a broad range of cluster sizes. The production of particles with the current best-matching radius of 20 nm is not fully understood from this picture. Smaller objects, specifically clusters Sn_n ($n = 6…40$), exhibit extinction cross section spectra,[29] dominated by absorption, which can produce broadband responses similar to the observed broadband component.

The much more violent process of homogeneous nucleation, which occurs when the liquid is heated close to thermodynamic critical temperature,[47] may well explain the formation of larger nanoparticles. Typical reported nanoparticles sizes resulting from homogeneous nucleation range of 5–25 nm[56–61] similar to the current observation. Homogeneous nucleation leads to rapidly expanding gas bubbles expelling nearby liquid mass and, thus, creating nanoparticles.[61] The used VP intensities in our experiment heat the thin film at a rate of approximately 10^{12} K/s. At these intensities and time scales, homogeneous nucleation has been observed previously.[62] The identification of the underlying vaporization mechanism is, thus, strongly intertwined with the origin of the broadband extinction spectrum. Future work could probe the thin-film vaporization process in a time-resolved manner, thereby enabling the separation of the two vaporization mechanisms, with the longest VP and shortest possible SP pulses maximizing the effective temporal resolution, employing the method introduced in this work.

In conclusion, we introduce an optical diagnostic method for characterizing the composition of a vapor based on UV spectroscopic absorption imaging. We use the method to study tin vapor created by irradiating a thin film with a laser; a case inspired by industrial LPP EUV sources. We obtain high-resolution images containing a high-resolution spectrum for the vapor in each pixel. Using our spectroscopic imaging method, we reveal a rather homogeneous temperature profile throughout the vapor, close to the boiling temperature of tin, and obtain a density map for atoms and nanoparticles, both of which are shown to be present in the vapor. For each free atom, several others appear to be clustered in nanoparticles and the composition appears to be frozen in. We combine the density and temperature maps for free atoms to obtain the electron density in the vapor, which is highly relevant to industrial applications. Finally, besides the clear value of our method to quantify tin vapor targets for industrial applications in EUV lithography and fusion alike, it may also provide more general insight into vapor production mechanisms under extreme conditions and can also be applied to broader studies of the dynamics of phase changes in free-standing thin films.

See the supplementary material for a video which animates Fig. 1 to show the evolution of the absorption images with backlight wavelength, as well as (Note 1) an overview Table S1 of the atomic transitions relevant to this work and (Note 2) details underlying Hertz–Knudsen calculations.

This work has been carried out at the Advanced Research Center for Nanolithography (ARCNL). ARCNL is a public-private partnership with founding partners UvA, VU, NWO-I, and ASML, and associate partner RUG. The authors thank Niek Lopes Cardozo, Michael Purvis, and Haining Wang for valuable discussions and ASML for loaning a laser system. We would also like to thank Henk-Jan Boluijt and Laurens van Buuren for their work on the experimental setup.

This research was funded by the European Research Council (No. ERC StG 802648) and the Nederlandse Organisatie voor Wetenschappelijk Onderzoek (No. OTP 19458).

AUTHOR DECLARATIONS

Conflict of Interest

The authors have no conflicts to disclose.

Author Contributions

Dion Junior Engels: Conceptualization (equal); Data curation (equal); Formal analysis (equal); Investigation (equal); Methodology (equal); Software (equal); Visualization (equal); Writing – original draft (equal); Writing – review & editing (equal). **Randy Anthonius Meijer:** Conceptualization (equal); Investigation (equal); Methodology (equal); Writing – review & editing (equal). **Hermann Karl Schubert:** Investigation (equal); Writing – review & editing (equal). **Wim J. Van der Zande:** Conceptualization (equal); Supervision (equal); Writing – review & editing (equal). **Wim Ubachs:** Conceptualization (equal); Investigation (equal); Methodology (equal); Supervision (equal); Writing – review & editing (equal). **Oscar Oreste Versolato:** Conceptualization (equal); Funding acquisition (equal); Investigation (equal); Methodology (equal); Supervision (equal); Writing – review & editing (equal).

DATA AVAILABILITY

The data that support the findings of this study are available from the authors upon reasonable request.

REFERENCES

[1]G. S. Yun, W. Lee, M. J. Choi, J. Lee, H. K. Park, B. Tobias, C. W. Domier, N. C. Luhmann, A. J. H. Donné, and J. H. Lee (KSTAR Team), Phys. Rev. Lett **107**, 045004 (2011).
[2]A. Perek, W. A. J. Vijvers, Y. Andrebe, I. G. J. Classen, B. P. Duval, C. Galperti, J. R. Harrison, B. L. Linehan, T. Ravensbergen, K. Verhaegh, M. R. de Baar, TCV, and EUROfusion MST1 Teams, Rev. Sci. Instrum. **90**, 123514 (2019).
[3]K. Verhaegh, B. Lipschultz, J. R. Harrison, N. Osborne, A. C. Williams, P. Ryan, J. S. Allcock, J. G. Clark, F. Federici, B. Kool, T. Wijkamp, A. Fil, D. Moulton, O. Myatra, A. Thornton, T. O. S. J. Bosman, C. Bowman, G. Cunningham, B. P. Duval, S. Henderson, R. Scannell, and MAST Upgrade Team, Nucl. Fusion **63**, 016014 (2022).
[4]T. A. Wijkamp, J. S. Allcock, X. Feng, B. Kool, B. Lipschultz, K. Verhaegh, B. P. Duval, J. R. Harrison, L. Kogan, N. Lonigro, A. Perek, P. Ryan, R. M. Sharples, I. G. J. Classen, R. J. E. Jaspers, and MAST Upgrade Team, Nucl. Fusion **63**, 056003 (2023).
[5]C. Wagner and N. Harned, Nat. Photonics **4**, 24 (2010).
[6]J. Scheers, R. Schupp, R. Meijer, W. Ubachs, R. Hoekstra, and O. O. Versolato, Phys. Rev. E **102**, 013204 (2020).
[7]F. Torretti, J. Sheil, R. Schupp, M. M. Basko, M. Bayraktar, R. A. Meijer, S. Witte, W. Ubachs, R. Hoekstra, O. O. Versolato, A. J. Neukirch, and J. Colgan, Nat. Commun. **11**, 2334 (2020).

04 January 2024 12:56:13

© Author(s) 2023

[8]V. Motto-Ros, Q. L. Ma, S. Grégoire, W. Q. Lei, X. C. Wang, F. Pelascini, F. Surma, V. Detalle, and J. Yu, Spectrochim. Acta Part B **74–75**, 11 (2012).
[9]H. J. van der Meiden, J. W. M. Vernimmen, K. Bystrov, K. Jesko, M. Y. Kantor, G. De Temmerman, and T. W. Morgan, Appl. Phys. Lett. **109**, 261102 (2016).
[10]V. N. Ochkin, S. Y. Savinov, S. N. Tskhai, U. Czarnetzki, V. S. von der Gathen, and H. F. Dobele, IEEE Trans. Plasma Sci. **26**, 1502 (1998).
[11]S. Hassaballa, M. Yakushiji, Y.-K. Kim, K. Tomita, K. Uchino, and K. Muraoka, IEEE Trans. Plasma Sci. **32**, 127 (2004).
[12]K. Tomita, Y. Sato, S. Tsukiyama, T. Eguchi, K. Uchino, K. Kouge, H. Tomuro, T. Yanagida, Y. Wada, M. Kunishima, G. Soumagne, T. Kodama, H. Mizoguchi, A. Sunahara, and K. Nishihara, Sci. Rep. **7**, 12328 (2017).
[13]K. Sakai, S. Isayama, N. Bolouki, M. S. Habibi, Y. L. Liu, Y. H. Hsieh, H. H. Chu, J. Wang, S. H. Chen, T. Morita, K. Tomita, R. Yamazaki, Y. Sakawa, S. Matsukiyo, and Y. Kuramitsu, Phys. Plasmas **27**, 103104 (2020).
[14]H. Mizoguchi, H. Nakarai, T. Abe, K. M. Nowak, Y. Kawasuji, H. Tanaka, Y. Watanabe, T. Hori, T. Kodama, Y. Shiraishi, T. Yanagida, G. Soumagne, T. Yamada, T. Yamazaki, S. Okazaki, and T. Saitou, Adv. Opt. Technol. **4**, 297 (2015).
[15]O. O. Versolato, Plasma Sources Sci. Technol. **28**, 083001 (2019).
[16]T. W. Morgan, P. Rindt, G. G. van Eden, V. Kvon, M. A. Jaworksi, and N. J. L. Cardozo, Plasma Phys. Controlled Fusion **60**, 014025 (2017).
[17]S. Roccella, G. Dose, R. de Luca, M. Iafrati, A. Mancini, and G. Mazzitelli, J. Fusion Energy **39**, 462 (2020).
[18]P. Rindt, J. L. van den Eijnden, T. W. Morgan, and N. J. L. Cardozo, Fusion Eng. Des. **173**, 112812 (2021).
[19]I. Fomenkov, D. Brandt, A. Ershov, A. Schafgans, Y. Tao, G. Vaschenko, S. Rokitski, M. Kats, M. Vargas, M. Purvis, R. Rafac, B. L. Fontaine, S. D. Dea, A. LaForge, J. Stewart, S. Chang, M. Graham, D. Riggs, T. Taylor, M. Abraham, and D. Brown, Adv. Opt. Technol. **6**, 173 (2017).
[20]I. Fomenkov, see https://www.euvlitho.com/2017/S1.pdf for "EUV source for high volume manufacturing: Performance at 250 W and key technologies for power scaling" (2017).
[21]B. Liu, R. A. Meijer, J. Hernandez-Rueda, D. Kurilovich, Z. Mazzotta, S. Witte, and O. O. Versolato, J. Appl. Phys. **129**, 053302 (2021).
[22]J. R. Freeman, S. S. Harilal, and A. Hassanein, J. Appl. Phys. **110**, 083303 (2011).
[23]T. Cummins, C. O'Gorman, P. Dunne, E. Sokell, G. O'Sullivan, and P. Hayden, Appl. Phys. Lett. **105**, 044101 (2014).
[24]D. Kurilovich, A. L. Klein, F. Torretti, A. Lassise, R. Hoekstra, W. Ubachs, H. Gelderblom, and O. O. Versolato, Phys. Rev. Appl. **6**, 014018 (2016).
[25]B. Liu, D. Kurilovich, H. Gelderblom, and O. O. Versolato, Phys. Rev. Appl. **13**, 024035 (2020).
[26]H. Gelderblom, H. Lhuissier, A. L. Klein, W. Bouwhuis, D. Lohse, E. Villermaux, and J. H. Snoeijer, J. Fluid Mech. **794**, 676 (2016).
[27]C. F. Bohren and D. R. Huffman, *Absorption and Scattering of Light by Small Particles* (Wiley, 1983), p. 530.
[28]R. M. Drake and J. E. Gordon, Am. J. Phys. **53**, 955 (1985).
[29]A. Lehr, F. Rivic, M. Jäger, M. Gleditzsch, and R. Schäfer, Phys. Chem. Chem. Phys. **24**, 11616 (2022).
[30]A. Kramida, Yu. Ralchenko, J. Reader, and NIST ASD Team, see https://physics.nist.gov/asd for "NIST Atomic Spectra Database (ver. 5.10)" (National Institute of Standards and Technology, Gaithersburg, MD, 2022); accessed August 25, 2023.
[31]R. C. Hilborn, Am. J. Phys. **50**, 982 (1982).
[32]C. J. Foot, *Atomic Physics* (Oxford University Press, 2005), p. 331.
[33]J. A. Aguilera and C. Aragón, Spectrochim. Acta, Part B **59**, 1861 (2004).
[34]J. Lambert, *Photometria Sive de Mensura et Gradibus Luminis, Colorum et Umbrae* (Eberhardt Klett, 1760).
[35]Beer, Ann. Phys. **162**, 78 (1852).
[36]R. Schupp, F. Torretti, R. A. Meijer, M. Bayraktar, J. Sheil, J. Scheers, D. Kurilovich, A. Bayerle, A. A. Schafgans, and M. Purvis, Appl. Phys. Lett. **115**, 124101 (2019).
[37]M. V. Romalis, E. Miron, and G. D. Cates, Phys. Rev. A **56**, 4569 (1997).
[38]S. Prahl, see https://miepython.readthedocs.io/en/v2.2.3/index.html for "Miepython—miepython 2.2.3 documentation" (2022).
[39]B. J. Sumlin, W. R. Heinson, and R. K. Chakrabarty, J. Quant. Spectrosc. Radiat. Transf. **205**, 127 (2018).
[40]R. Kofman, P. Cheyssac, and R. Garrigos, Phase Transit. **24–26**, 283 (1990).
[41]A. Lehr, M. Jäger, and R. Schäfer, J. Phys. Chem. C **124**, 1070 (2020).
[42]G. Cisneros, J. S. Helman, and C. N. J. Wagner, Phys. Rev. B **25**, 4248 (1982).
[43]P. Drude, Ann. Phys. **306**, 566 (1900).
[44]H. R. Griem, *Principles of Plasma Spectroscopy*, Cambridge Monographs on Plasma Physics (Cambridge University Press, 1997).
[45]M. M. Basko, V. G. Novikov, and A. S. Grushin, Phys. Plasmas **22**, 053111 (2015).
[46]M. M. Martynyuk, Russ. J. Phys. Chem. **57**, 494 (1983).
[47]A. Miotello and R. Kelly, Appl. Phys. Lett. **67**, 3535 (1995).
[48]R. Kelly and A. Miotello, Appl. Surf. Sci. **96–98**, 205 (1996).
[49]A. Miotello and R. Kelly, Appl. Phys. A **69**, S67 (1999).
[50]N. M. Bulgakova and A. V. Bulgakov, Appl. Phys. A **73**, 199 (2001).
[51]A. H. A. Lutey, J. Appl. Phys. **114**, 083108 (2013).
[52]J. Safarian and T. A. Engh, Mettal. Mater. Trans. A **44**, 747 (2013).
[53]D. R. Stull, Ind. Eng. Chem. **39**, 517 (1947).
[54]J. A. Cahill, G. M. Krieg, and A. V. Grosse, J. Chem. Eng. Data **13**, 504 (1968).
[55]D. A. Young and B. J. Alder, Phys. Rev. A **3**, 364 (1971).
[56]C. Liang, Y. Shimizu, T. Sasaki, and N. Koshizaki, J. Phys. Chem. B **107**, 9220 (2003).
[57]S. Amoruso, G. Ausanio, R. Bruzzese, M. Vitiello, and X. Wang, Phys. Rev. B **71**, 033406 (2005).
[58]P. T. Murray and E. Shin, Mater. Lett. **62**, 4336 (2008).
[59]J. C. Alonso, R. Diamant, P. Castillo, M. C. Acosta-García, N. Batina, and E. Haro-Poniatowski, Appl. Surf. Sci. **255**, 4933 (2009).
[60]A. Mazzi, F. Gorrini, and A. Miotello, Phys. Rev. E **92**, 031301 (2015).
[61]A. Mazzi and A. Miotello, J. Colloid Interface Sci. Laser Synth. **489**, 126 (2017).
[62]A. Mazzi, F. Gorrini, and A. Miotello, Appl. Surf. Sci. **418**, 601 (2017).

04 January 2024 12:56:13

© Author(s) 2023